Research Article

Synthesis, characterization and dielectric studies of poly(1-naphthylamine)–tungsten disulphide nanocomposites

Femina Kanjirathamthadathil Saidu[1,2] · **George Vazhathara Thomas**[1]

Received: 6 December 2019 / Accepted: 6 April 2020 / Published online: 3 June 2020

Abstract

Here, novel poly(1-naphthylamine)–tungsten disulphide (PNA–WS_2) nanocomposites were synthesized through an in-situ chemical oxidative polymerization of 1-naphthylamine in the presence of ultrasonically dispersed WS_2. The effect of WS_2 addition on the optoelectrical, morphological and thermal properties of PNA was studied by using different analytical tools. SEM images revealed that PNA aggregates are well supported on the dispersed WS_2 sheets. The formation of a fibrous network of PNA over the dispersed WS_2 layers evidenced from the TEM images has suggested larger surface area and better interfacial interaction between PNA and incorporated WS_2 layers. The thermal stability was improved upon the incorporation of WS_2. Optical bandgap values of PNA–WS_2 nanocomposites were lower than that of bulk WS_2 and pristine PNA. Electrical and dielectric studies have confirmed an improvement in conductivity and dielectric properties with increasing WS_2 content, which was credited to the better charge transport between the polar backbone of PNA and charged surface of dispersed WS_2 due to enhanced interfacial area and electrostatic interactions between the components. A maximum AC conductivity of 4.4×10^{-3} Sm^{-1} was displayed by nanocomposite containing 20% WS_2 loading and a further increase in WS_2 content showed a detrimental effect in electrical and dielectric properties. The present study has demonstrated that optical and dielectric properties of composites can be readily tuned by proper control of the composition and dispersion of WS_2 within the PNA matrix.

Electronic supplementary material The online version of this article (https://doi.org/10.1007/s42452-020-2889-7) contains supplementary material, which is available to authorized users.

✉ George Vazhathara Thomas, georgevtsjc@gmail.com | [1]Department of Chemistry, St. Joseph's College, Moolamattom, Idukki, Kerala 685591, India. [2]Department of Chemistry, Maharaja's College, Ernakulam, Kerala 682011, India.

Graphic abstract

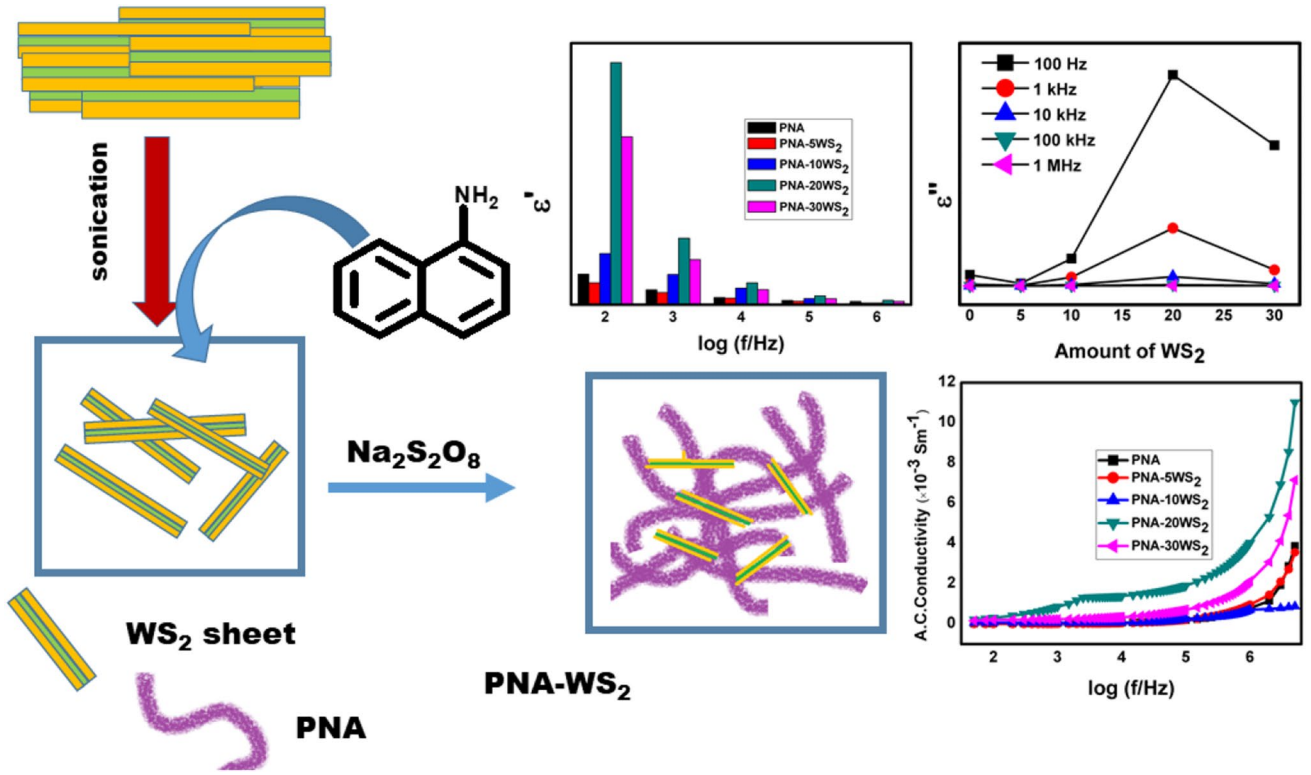

Keywords Inorganic graphene analogues · Nanocomposite · Dielectric · Conducting polymer

1 Introduction

Inorganic graphene analogues (IGAs) are a new class of 2D nanomaterials having distinctive properties and applications and their composites are widely explored in recent time [1–4]. Of the IGAs, WS_2 is a unique member with impressive electrical, magnetic and optical attributes [5–12]. WS_2 shows layer dependent direct bandgap, photoluminescence and electron transport properties [13–15]. Because of its broad application potentials, scientists have adopted different methods like chemical exfoliation, liquid-phase exfoliation, sonochemical methods and hydrothermal method for preparing nano-sized IGAs [16–20]. The ultrasound-assisted mechanical exfoliation of bulk WS_2 is a simple and economical method compared to chemical exfoliation. Effective incorporation of IGAs over a support matrix could show excellent performance in their catalytic and sensor applications [21–24].

For miniaturized electronic devices, materials with exceptional dielectric properties are required [25–28]. IGA based dielectrics and capacitors are attractive due to their ease of synthesis, low cost and high stability. Polymeric dielectrics are attractive as they have high dielectric breakdown field strength along with the additional advantage of processability, flexibility and chemical stability, but dielectric permittivity of polymers is low [29–31]. Conjugated polymers (CPs) are a particular category of macromolecules with highly polar structure and conjugated backbone, which are gaining more academic interest as the dielectric materials. The CPs have comparatively higher dielectric constant than that of common thermoplastic or thermosetting polymers owing to their highly polarizable conjugated backbone [32–35]. By using CPs as the polymer matrix for dispersing nanomaterials, the dielectric properties of the individual components can be integrated effectively. The materials having high dielectric permittivity and low dielectric loss are suitable for energy storing applications. CP based dielectric materials have high dielectric breakdown field strength along with better processability, flexibility and resistance to chemical attack [36, 37]. IGA-CP nanocomposites have improved conductivity along with better capacitance, mechanical strength and

thermal stability [38, 39]. Therefore, IGA-CP composites are attractive for the fabrication of flexible, thin, lightweight and low-cost organic electronics for electronic displays, sensors and solar technologies.

Polyaniline (PANI) is a unique CP, and its dielectric and capacitance studies have been extensively reported [37, 40–44]. Poly(1-naphthylamine) (PNA) is a PANI derivative which is gathering immense attraction among the research communities in recent years. Compared to PANI, PNA is highly processable and thermally stable. PNA has excellent electrochromic, photocatalytic and electrocatalytic properties owing to its low bandgap and unique structural features [45–54]. This work was focused on the preparation of lightweight and low-cost functional materials by hybridizing the unique properties of semiconducting PNA and layered WS_2. The effect of WS_2 loading on thermal, electrical and optical properties was also studied. The dielectric behaviour and AC conductivity of the prepared nanocomposites were studied within the frequency range of 50 Hz–1.5 MHz. It is the first report on the dielectric properties of the PNA, and its composites and the finding of this study suggests that efficient and highly processable materials for EMI shielding or microwave absorbing applications can be derived from the similar PNA based systems.

2 Experimental

2.1 Materials

WS_2 powder, ammonium peroxodisulphate $(NH_4)_2S_2O_8$), concentrated hydrochloric acid (HCl) were of analytical grade and supplied by Merck, India. The monomer 1-naphthylamine ($C_{10}H_7NH_2$) was purchased from Loba Chemie, India, and it was recrystallized from ethanol before use. Deionized water and distilled ethanol were used as solvents for the study.

2.2 Preparation of PNA–WS_2 nanocomposites

PNA was synthesized by adding APS to the solution of NA in 1 M HCl by following the method described in our previous work [55]. Accurately weighed amount of bulk WS_2 powder was transferred into 100 mL of 1 M HCl solution in a beaker and ultra-sonicated for an hour using a probe sonicator. A definite amount of alcoholic solution of NA was added to the above dispersion. It was again sonicated in a bath for 30 min. A solution of ammonium peroxodisulphate (APS) in 1 M HCl (1:1 M) was added slowly within half an hour to the above mixture. The colour of the solution turned dark blue within a few minutes, indicating the polymerization of NA. Stirring was continued for 3 h at room temperature. The mixture was kept undisturbed overnight. Filtered and washed until the filtrate was colorless. The purple-blue solid obtained was dried at 60 °C in a vacuum for 6 h. The same procedure was repeated by varying the composition of WS_2 and NA. The prepared composites were designated as PNA–5WS_2, PNA–10WS_2, PNA–20WS_2 and PNA–30WS_2 which contains 5%, 10%, 20% and 30% WS_2 loading, respectively.

2.3 Characterization

The FTIR spectra of synthesized PNA and PNA–WS_2 nanocomposites were recorded in the region of 400–4,000 cm^{-1} using NICOLET FT-IR Thermo scientific spectrometer. The X-ray diffraction patterns of synthesized PNA, WS_2 and PNA–WS_2 samples were recorded in the 2θ range between 3° and 80° with CuKα radiation ($\lambda = 1.5418$ Å) at a scan rate of 0.05°s^{-1} using Bruker AXS D8 Advance diffractometer. Morphological studies were carried out with SEM analysis using VEGA 3TESCAN instrument. HRTEM images of PNA–WS_2 nanocomposite were recorded using a JEOL JEM 2100 electron microscope. Thermogravimetric studies were performed using Perkin Elmer STA 6000 within the temperature range from 40 to 750 °C at 10 °C min^{-1} under N_2 atmosphere. The surface elemental composition was determined by energy dispersive X-ray analysis (OXFORD XMX N, UK). UV–Vis diffuse reflectance spectroscopy (DRS) spectra were recorded using powdered samples in the range of 200–800 nm (SHIMADZU UV-2600, Japan). Direct current (DC) conductivity measurements were conducted using pressed pellets. The pellets of 13 mm diameter and 1–2 mm thickness were made using hydraulic press by applying a pressure of 5 torr. The DC conductivity of the polymer and its composites were studied using Keithely2450 four-probe conductivity meter. For electrical contacts, both faces of the pellet were evenly coated with a thin layer of silver paste. Dielectric and AC conductivity of these pelletized samples were measured using a programmable HIOKI 3250-50 LCR meter in the frequency range of 50 Hz–1.5 MHz. The conductivity and dielectric measurements were done at room temperature (30 °C). The real part of the complex dielectric permittivity ($\boldsymbol{\varepsilon'}$) of the material was calculated using the formula $\boldsymbol{\varepsilon' = Cd/\varepsilon_o A}$, where C is the capacitance, d is the thickness (m), A is the area (m^2), and $\boldsymbol{\varepsilon_o}$ is the permittivity of free space. The imaginary part of the complex dielectric permittivity (dielectric loss) ($\boldsymbol{\varepsilon''}$) was calculated using the relation $\boldsymbol{\varepsilon'' = \varepsilon' D}$, where 'D' is the dissipation factor. AC conductivity of prepared systems was calculated as $\boldsymbol{\sigma_{ac} = 2\pi f \cdot D \cdot \varepsilon_o \cdot \varepsilon_r'}$ where '$\boldsymbol{\varepsilon_r'}$' is the relative permittivity and 'f' is the applied frequency (Hz).

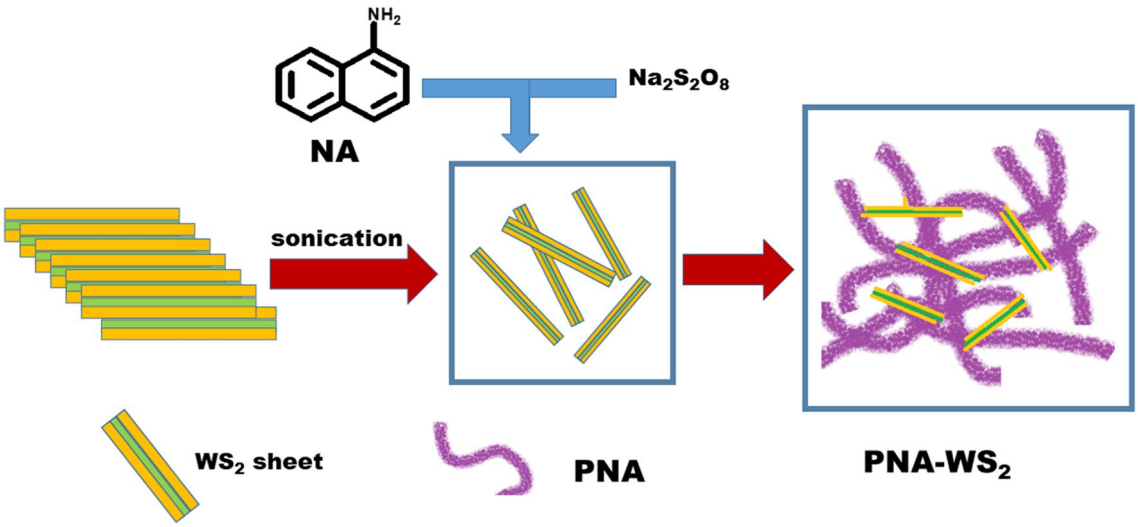

Fig. 1 Scheme of formation of PNA–WS_2 nanocomposites

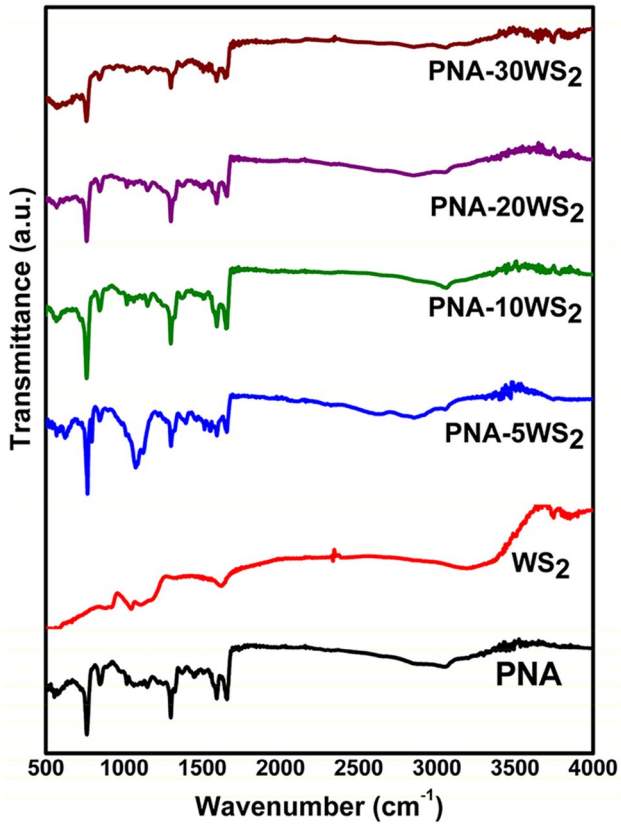

Fig. 2 FTIR of PNA, WS_2 and PNA–WS_2 nanocomposites

3 Results and discussion

3.1 Formation of PNA–WS_2 nanocomposites

Here, PNA was prepared via a simple chemical oxidative polymerization of NA in acidic medium. The scheme of oxidative polymerization of NA is shown in Fig. S1(supplementary data). PNA–WS_2 nanocomposites were prepared through in-situ polymerization. It is suggested that during the mixing of an acidic solution of NA with ultrasonically dispersed WS_2, the positively charged protonated NA ions are get adsorbed on to the negatively charged surface of WS_2. On adding APS solution to this dispersion, polymerization of NA to PNA takes place, and PNA chains are intercalated between partially exfoliated WS_2. The schematic representation of the formation of intercalated PNA–WS_2 composites is shown in Fig. 1.

3.2 FTIR studies

FTIR spectra of PNA, WS_2 and its nanocomposites are shown in Fig. 2. IR spectrum of WS_2 has a broad and less intense peaks which are in good agreement with IR data of bulk WS_2 reported earlier [56–58]. IR spectra of PNA and its WS_2 nanocomposites show peaks around 3400 cm^{-1} due to the imine N–H stretching vibrations [59]. The N–H peaks observed were broad due to extensive hydrogen bonding between –NH group and the solvent molecules. Intense peaks in the range of 764–761 cm^{-1} observed for pristine PNA and its composites originated from the C–H deformation of the 1, 4 coupled NA confirmed the polymerization through the C(4)–N coupling of NA units [49, 50, 60]. Presence of intense peaks suggest that the degree of polymerization is not affected by the presence of WS_2.The peaks correspond to imine stretching vibration are slightly shifted from 1654 cm^{-1} for PNA to 1657 cm^{-1} for PNA–WS_2 composites. Additionally, C–H deformation absorption at 1084 cm^{-1} further confirmed the polymerization as proposed by Ameen et al. Other prominent peaks

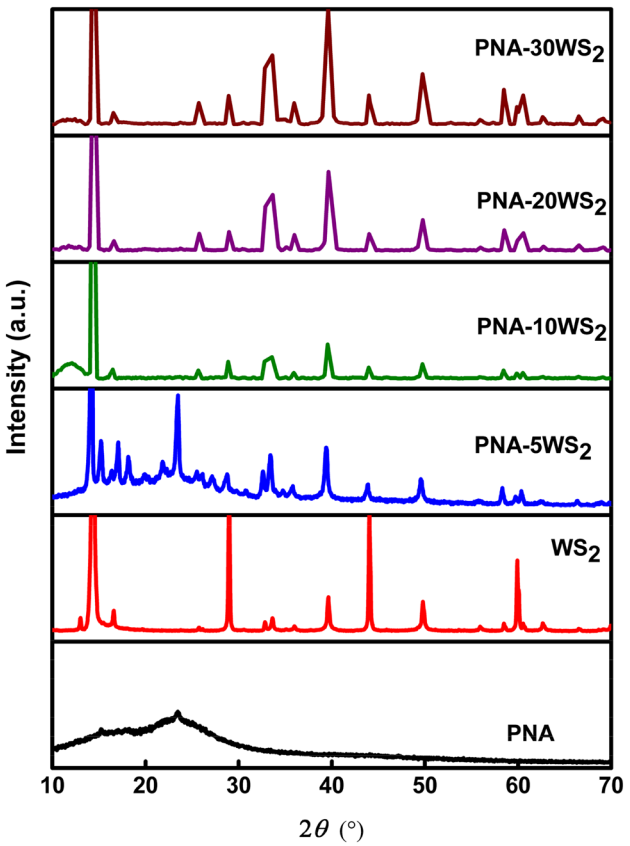

Fig. 3 XRD pattern of PNA, WS_2 and PNA–WS_2 nanocomposites

at around 1655 cm^{-1}, 1589 cm^{-1}, 1309 cm^{-1}, 1151 cm^{-1} were assigned to the imine stretching, quinoid stretching, aromatic C–N stretching and benzenoid–NH–quinoid stretching, respectively. A noticeable variation in the relative intensities of the benzenoid and quinonoid vibrational peaks was observed during the incorporation of WS_2 into the PNA matrix suggesting active interfacial interaction WS_2 layers and the polymer chain which may affect its electronic structure and polymer characteristics.

3.3 XRD studies

The crystalline nature of WS_2 incorporated PNA composites was interpreted from the XRD data shown in Fig. 3. XRD pattern of PNA presented in Fig. 3 (black)contained a broad hump with few less intense peaks at 17° and 24° corresponds to the reflection from the [200], [020] planes of PNA indicating that HCl doped PNA emeraldine salt is semi-crystalline [61]. XRD pattern of bulk WS_2 (Fig. 3 red) confirm the layered structure of WS_2 which is evidenced from the characteristic peaks placed at $2\theta = 14.5°$, 29.8°, 33.5°, 36°, 40°, 44°, 50°, 58.5°, 60° corresponds to the crystal planes[002], [100], [101], [102], [103], [006], [105], [110], [112] of hexagonal 2H–WS_2, respectively (JCPDF-01–084-139:ICSD.202366) [62–64]. We have incorporated sheets of WS_2 dispersed by ultra-sonication. It is seen from the XRD results that the diffractions from the exfoliated nanosheets in PNA–WS_2 composite are comparable to the bulk form that corresponds to the hexagonal phase of WS_2. According to Mao et al., the observation of prominent [002] diffraction peak in all XRD patterns indicates the growth of WS_2 layers along the c-axis direction [9, 65]. Notably, the (002) peak for the PNA–WS_2 composites decreased in intensities and are broader when compared to the bulk WS_2, which may be caused by the decrease of structural crystallinity and the increase in the disorder density. It is deducted from the XRD studies that the layered structure of WS_2 is kept intact during the nanocomposite formation suggesting that PNA is intercalated within the interlayer galleries of WS_2.

However, in the XRD patterns of PNA–WS_2 nanocomposites, the diffraction from PNA becomes comparatively less intense, suggesting the amorphous nature of the formed PNA. The change in crystallinity is possible as WS_2 layers may intervene in the intra-chain interaction and their orderly stacking of PNA. In case of low WS_2 loading, say 5% WS_2, a large bump which extends over $2\theta = 10–30°$ with a few less intense peaks are observed suggesting that periodicity of PNA is maintained to some extent at lower loading. As per the previous reports, small peaks around $2\theta = 6$, 9, 14°, 17° and 23° are related to the (020), (010), (200), (100) and (011) planes of the pseudo-orthorhombic lattice of PNA [50, 66, 67]. As WS_2 loading increases, the reflection from the PNA becomes insignificant. Hence, it is suggested that upon incorporation of WS_2 the orientation of polymer considerably affected and the PNA chains with short-range orders are randomly distributed over WS_2. For PNA–WS_2 nanocomposites except for PNA–5WS_2, only an amorphous hump is observed at $2\theta < 13°$, which is correlated to the [200] reflection of PNA and additionally, characteristic peaks of PNA gradually diminished in intensity. A profoundly intense peak at around $2\theta = 14°$ is observed in the XRD pattern of all nanocomposites that is connected to the reflection from [002] plane of WS_2, suggesting that formation of polymer intercalated composites and similar results were reported elsewhere [58, 63]. Based on the XRD results it is concluded that the orientation and crystal structure of the PNA was considerably varied during composite formation while that of WS_2 remains almost intact. This assumption was further supported by morphological studies using electron microscopic methods.

3.4 SEM studies

SEM images of PNA, bulk WS_2, PNA–10WS_2 and PNA–20WS_2 are presented in Fig. 4. The HCl doped PNA appeared as aggregates of regular micro/nano globules

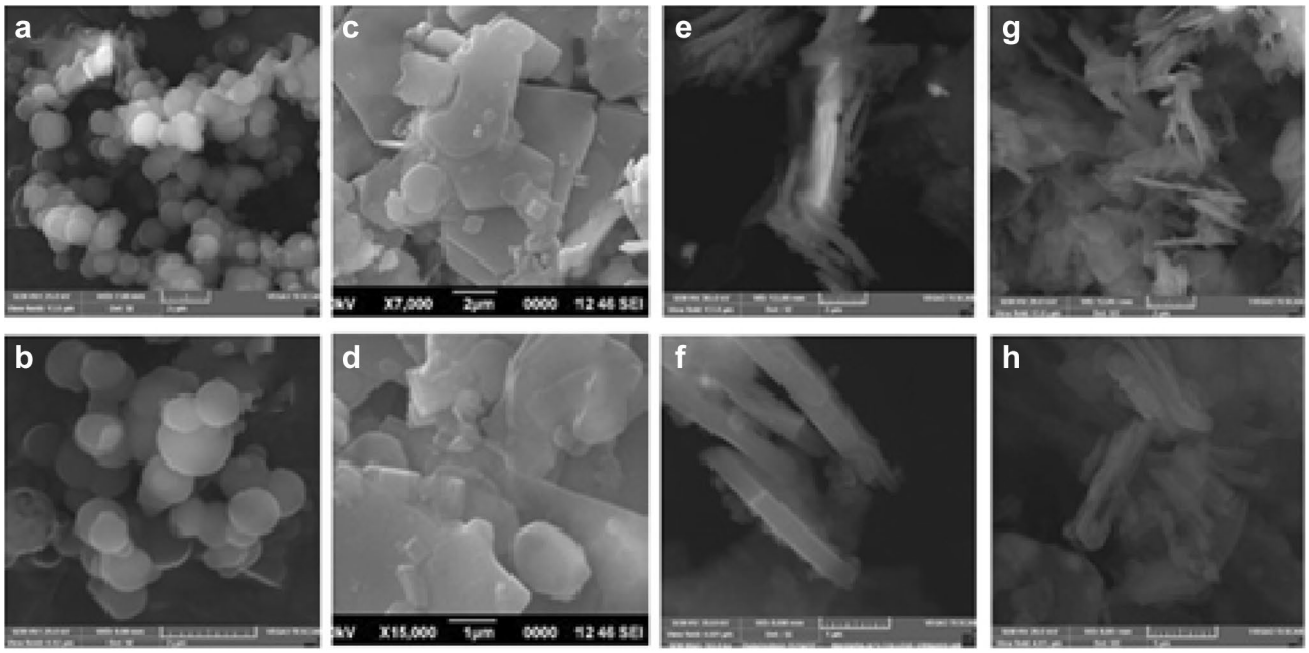

Fig. 4 SEM images under different magnification of PNA (**a**, **b**), WS_2 (**c**, **d**), PNA–10WS_2 (**e**, **f**) and PNA–20WS_2 (**g**, **h**)

(Fig. 4a, b), while the flake-like morphology of WS_2 was clear from its SEM images (Fig. 4c, d). On loading the exfoliated WS_2 sheets into the PNA matrix, there was a noticeable change in the morphology (Fig. 4e–h). Thin flakes of WS_2 are visible in the SEM pictures of the nanocomposites, and the filler WS_2 appears to be in a few-layer stacked condition. PNA globules adhered to the WS_2 sheets were seen in the SEM images of nanocomposites. It is possible as the WS_2 layers readily adsorb the HCl doped NA molecules due to electrostatic interactions. SEM study confirms the

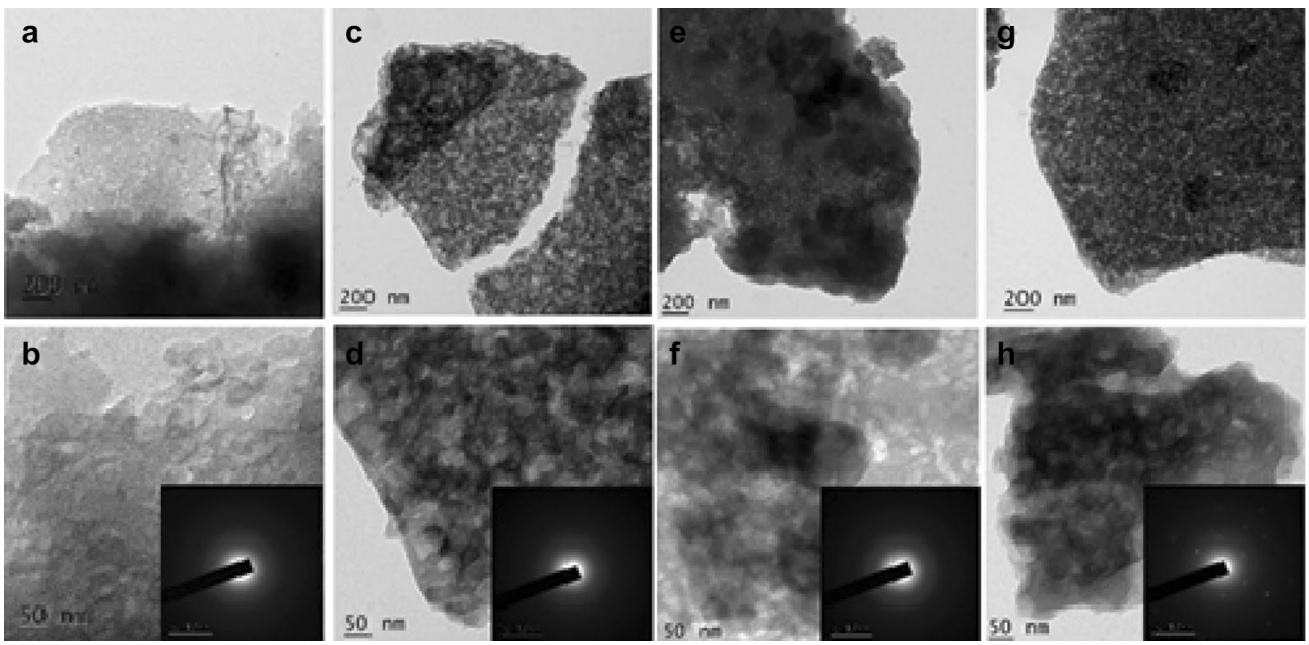

Fig. 5 TEM images under different magnification of PNA (**a**, **b**) PNA–5WS_2 (**c**, **d**), PNA–10WS_2 (**e**, **f**), PNA–20WS_2 (**g**, **h**) and their SAED patterns (inset **b**, **d**, **f** and **h**)

formation of PNA intercalated layered WS_2 nanocomposites during the in-situ polymerization. Thus, as proposed by XRD studies, it was concluded that amorphous PNA molecules were occupying in the cavities of ultrasonically exfoliated WS_2 sheets in addition to its surface yielding hybrid composites having intimate contact between components. Hence, it is anticipated that such arrangements can facilitate better charge transfer at the interface and hence could be a better candidate for catalysis and electrochemical capacitors. This could be because of the electrostatic interaction between the HCl doped NA molecules and negatively charged WS_2 layers.

3.5 TEM studies

Detailed information regarding the arrangement of PNA and WS_2 in the nanocomposites was gained from TEM studies. TEM images of PNA, PNA–5WS_2, PNA–10WS_2 and PNA–20WS_2 are shown in Fig. 5. TEM images of PNA (Fig. 5a, b) indicate that the PNA has a dispersed network structure and SAED pattern (inset Fig. 5b) further confirms that PNA was amorphous. However, in the TEM photographs of nanocomposites, the PNA has well defined fibrous network topology, and PNA nanostructures were appeared to be well supported on the hexagonal WS_2 sheets. TEM studies also reveal that layered WS_2 could homogenously distribute PNA on the exterior and also in between the layers, giving the maximum surface area with intimate interaction between the components. There was no apparent crystalline character observed for PNA–5WS_2 and PNA–10WS_2, as revealed by the diffusive circles in their SAED patterns (inset Fig. 5 d, f, respectively). Hence it was suggested that at lower WS_2 loading, efficient exfoliation was possible under ultrasonication and the intercalated PNA chains could effectively block the restacking of WS_2.

Table 1 Compositional details of PNA–WS_2 nanocomposites obtained from EDAX studies

Composite	wt% of W	wt% of S	at.% of W	at.% of S
PNA–5WS_2	1.51	1.2	0.1	0.48
PNA–10WS_2	4.32	1.65	0.31	0.68
PNA–20WS_2	9.68	1.71	0.81	0.97
PNA–30WS_2	17.28	3.04	1.45	1.46

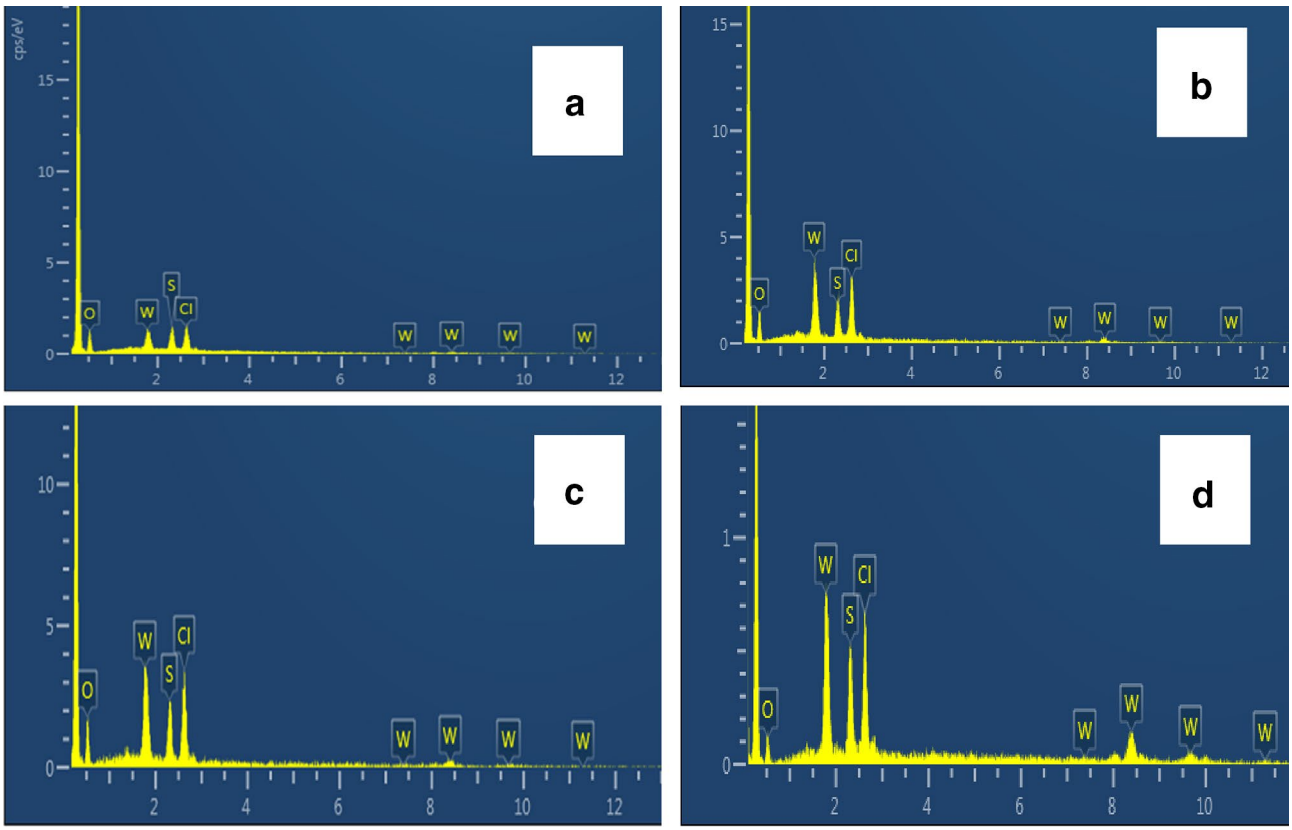

Fig. 6 EDAX pattern of PNA–5WS_2 (**a**) PNA–10WS_2 (**b**) PNA–20WS_2 (**c**) and PNA–30WS_2 (**d**)

The SAED pattern of the PNA–20WS_2 shows bright spots corresponds to the hexagonal WS_2 lattice, which is consistent with XRD results (inset Fig. 5h). The comparison of the SAED patterns of the nanocomposites discloses an increase in crystalline character with an increase in the WS_2 amount, which might be due to a high tendency for the restacking of WS_2 layers. Similar agglomeration of layered fillers in CP-IGA nanocomposites has been reported earlier [63, 68].

3.6 EDAX analysis

The chemical composition of the PNA–WS_2 composites is analyzed using EDAX analysis and corresponding EDAX spectra of PNA–5WS_2, PNA–10WS_2, PNA–20WS_2 and PNA–30WS_2 are shown in Fig. 6 a–d, respectively.

The amount of W and S in the composites detected by EDAX is presented in Table.1 The observed filler loading is lower than the theoretical value. It may be because of the semi-quantitative nature of the EDAX technique, which measures the composition of the exterior of the samples. Another reason for the observed lower WS_2 content may be due to the wrapping of WS_2 layers by PNA, as revealed by electron microscopic studies discussed in the previous sessions.

3.7 UV–Vis studies

The influence of WS_2 incorporation in the electronic spectra and optical properties of the PNA was studied using diffuse reflectance UV–Visible spectra (Fig. 7). The absorption spectra of PNA (Fig. 7a) and its nanocomposites (Fig. 7c–f) shows two observable humps, one in UV and other in the visible region. The peak in the UV region is attributed to the π–π^* transmission and later corresponds to polaronic transition. There is a considerable red shift in peak maxima for both electronic transitions. The π–π* absorption shifts from 315 to 340 nm and the n–π^* polaronic absorption from 521 to 540 nm. The broadness of the polaronic transition has a direct correlation to the extent of delocalization, and it has been influenced by WS_2 loading, as seen from the UV–Visible spectra. The UV–Visible spectrum of WS_2 powder is shown in Fig. 7b, and it displays four prominent peak maxima at wavelength 297, 376, 503 and 603 nm, and these results are consistent with earlier reports. Conclusively, it is clear from the spectral studies that the formation of intercalated nanocomposites has significantly affected the electronic band structure and, consequently, optical properties of the nanocomposites. The intensity and width of the polaronic absorption vary on the addition of WS_2, and larger width and intensity are observed for the PNA–10WS_2 and PNA–20WS_2 nanocomposites. The visible band found for PNA–10WS_2 is broader than that of other systems suggesting the extent of conjugation is better for PNA–10WS_2 compared to remaining nanocomposites. However, on further increasing WS_2 content, there observed a slight narrowing of the absorption hump. Therefore, based on the optical study, optimum charge transfer interactions offering maximum polaronic delocalization are anticipated for these nanocomposites. Upon increasing the loading of semiconducting WS_2, there may not be effective charge transfer between the randomly organized PNA because of the intervening WS_2 sheets. Thus, the electronic spectral studies reveal that PNA chain conformation and interfacial interactions are presumed to be affected by the loading and distribution of WS_2.

The direct bandgap values of WS_2, PNA and PNA–WS_2 nanocomposites were calculated from the Tauc's plot between $(ah\upsilon)^2$ versus photon energy ($h\upsilon$) in eV, where 'a' stands for the optical absorption coefficient and photon energy in eV can be calculated form wavelength using the equation $h\upsilon = 1240/\lambda$ presented in Fig. 8a–f. The allowed direct bandgap of prepared PNA and its WS_2 nanocomposites are obtained by extrapolating the straight-line portion of the plots to X-axis at zero $(ah\upsilon)^2$ value. The bandgap values of prepared systems were presented in Table 2. The band gap for HCl doped PNA was found to be 1.91 eV, and that of pure WS_2 was 2.14 eV. It is observed that all PNA–WS_2 nanocomposites have lower bandgap than both pure components, and the smallest of 1.77 eV was observed for PNA–10WS_2 nanocomposite. The bandgap values lie in the visible regime; hence, the intercalated PNA–WS_2 nanocomposites would be promising in solar-driven photocatalytic and photovoltaic applications. The study reveals that the band structure and band gap values can be engineered by incorporating WS_2 layers.

3.8 Thermal studies

Thermal stability and polymer degradation were studied using thermogravimetric analysis (TGA). From the TGA and DTG plots shown in Fig. 9a, b respectively, it is clear that all systems except pristine WS_2 have an initial weight loss at around 100 °C, which is attributed to the loss of adsorbed water molecules. Bulk WS_2 is highly stable and has not undergone appreciable weight loss up to 750 °C. For PNA,

Table 2 λ_{max} and band gap values of WS_2, PNA and all PNA–WS_2 nanocomposites

System	λ_{max} (nm)		Band gap (eV)
	π–π^* transition	Polaronic transition	
PNA	317	515	1.91
WS_2	297,376	513,611	2.14
PNA–5WS_2	331	523	1.89
PNA–10WS_2	335	534	1.77
PNA–20WS_2	338	544	1.83
PNA–30WS_2	340	540	1.81

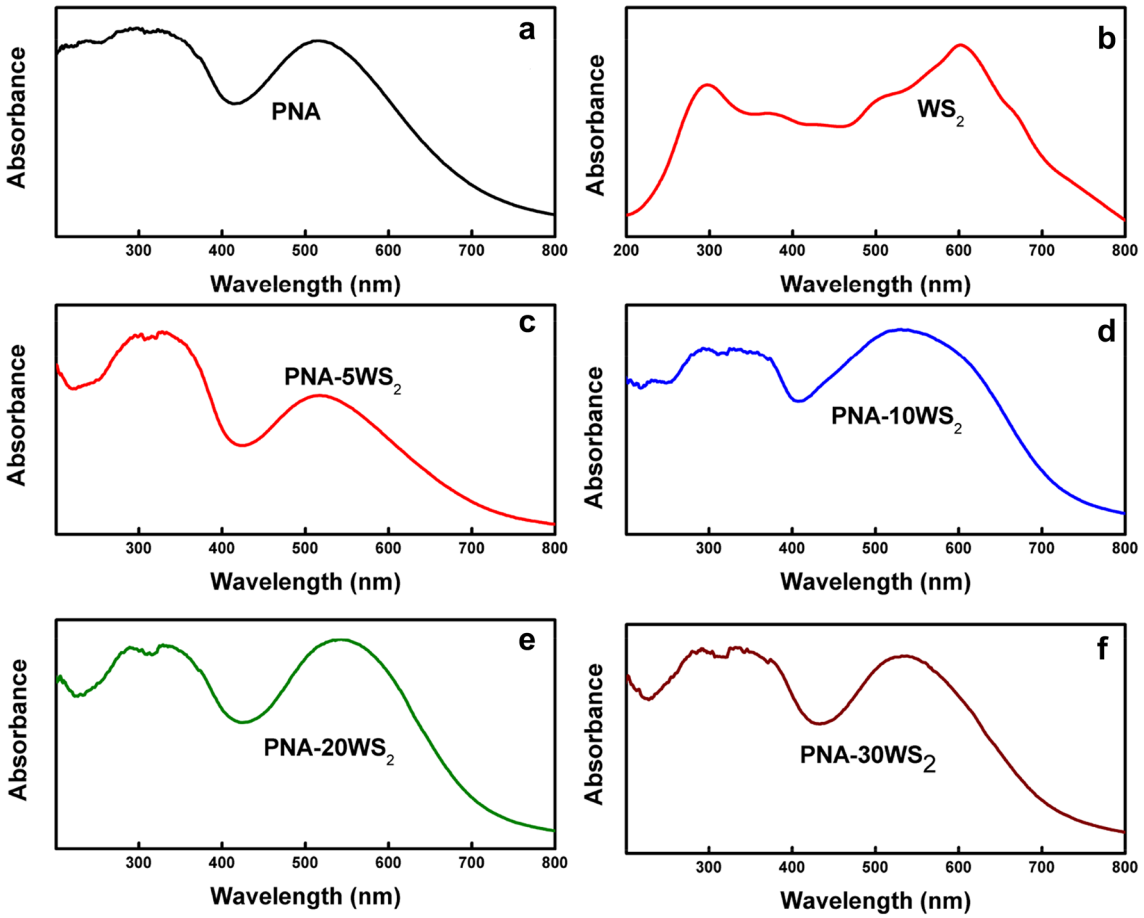

Fig. 7 UV–Visible Spectra of WS_2, PNA and PNA–WS_2 nanocomposites

a gradual weight loss observed in the temperature range of 175–250 °C is ascribed to the loss of dopant chloride ions along with the deprotonation of PNA chains. Around 320 °C, a gradual weight loss at a low rate has been observed for PNA and PNA–WS_2 composites suggesting the degradation of low molecular weight fractions along with the removal of co-intercalated chloride and interstitial water molecules. For PNA–5WS_2 weight loss occurs at a comparatively lower temperature, this could be due to the fast degradation of microcrystals of oligomeric PNA formed as indicated by its XRD spectrum. Above 530 °C, relatively faster weight loss was observed, which is attributed to PNA chain degradation. It is observed the polymer chains degradation temperature of nanocomposites increases with an increase in WS_2 loading. It is proposed that because of the interfacial interactions between the PNA chains and WS_2 layers due to efficient intercalation of PNA between the WS_2 sheets, the PNA chain degradation is inhibited. Thermal studies revealed that the WS_2 intercalated PNA backbone is less susceptible to degradation compared to bare PNA and the prepared PNA–WS_2 composites show enhanced thermal stability compared to similar IGA-PANI composites reported earlier [58, 69].

3.9 DC Conductivity

The DC conductivity values of all the prepared materials are presented in Fig. 10 and it is clear from the study that their conductivity lies in the semiconducting regime. DC conductivity for HCl doped PNA at 303 K was 5.4×10^{-5} Sm^{-1}. The low conductivity of PNA is due to its constraints to attain planarity because of the presence of large fused aromatic rings [60, 70]. All the WS_2 nanocomposites show an increase in DC conductivity and among the nanocomposites, better conductivity was observed for PNA–20WS_2. The increase in DC conductivity of nanocomposite is attributed to the doping effect of WS_2 layers which facilitate charge transport. Such an increase in conductivity of IGA incorporated conducting polymers composites was reported earlier. According to earlier reports, some synergistic interactions involving Lewis acid–base type coupling between the aromatic π-cloud and semiconducting metal sulfide layers that lead to the active charge transport between and across the intercalated PNA and WS_2 layers are possible, and hence conductivity is improved [71–73]. PNA–20WS_2 has shown the best electrical and

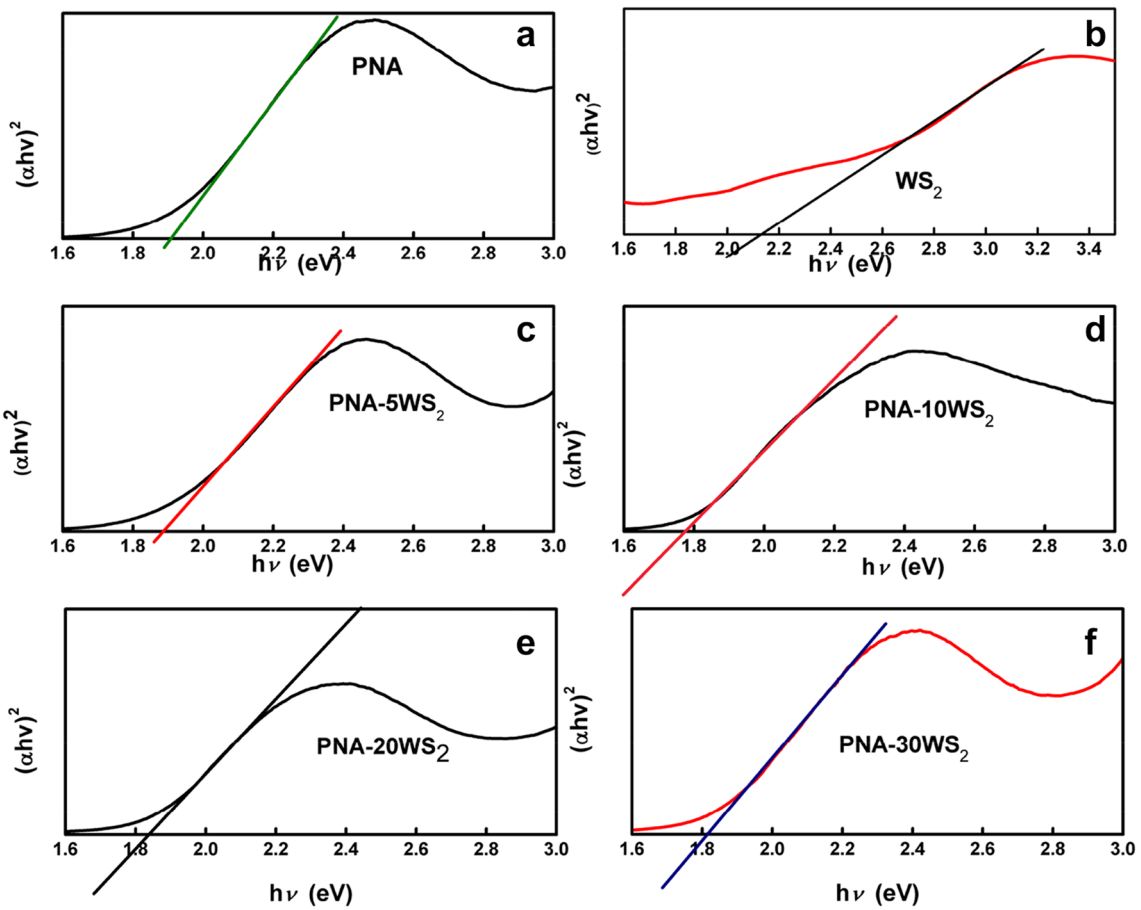

Fig. 8 Tauc's plots of WS_2, PNA and PNA–WS_2 nanocomposites

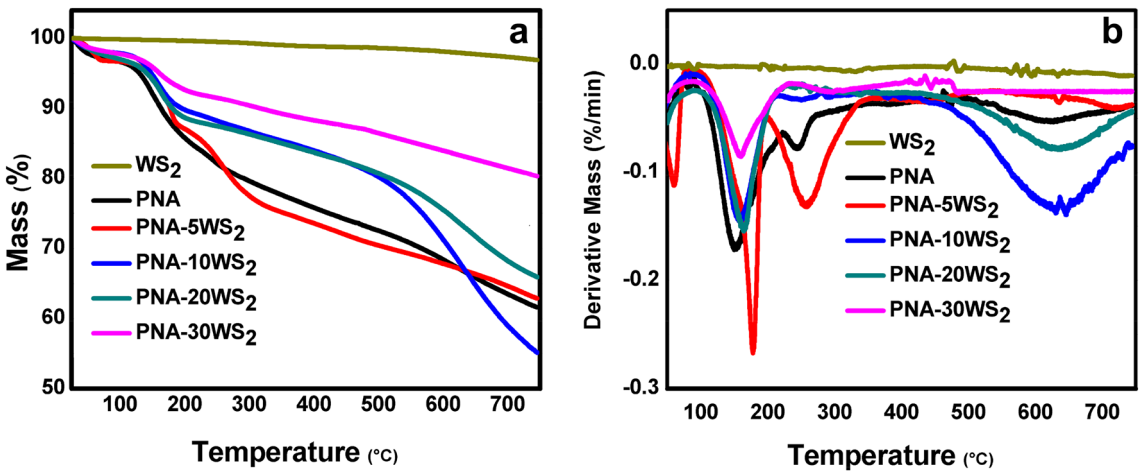

Fig. 9 TGA (**a**) and DTG (**b**) plots of PNA, WS_2 and PNA–WS_2 nanocomposites

optical characteristics among the prepared nanocomposites, which may be because of the optimum interfacial interactions between PNA and WS_2 sheets. As proposed by Sun et al. observed a decrease in conductivity on higher loading of WS_2 sheets, maybe because of the irregular orientation of component PNA and WS_2 sheets resulting in the poor interconnection between the conductive chains damaging the regularity and continuity hindering electron

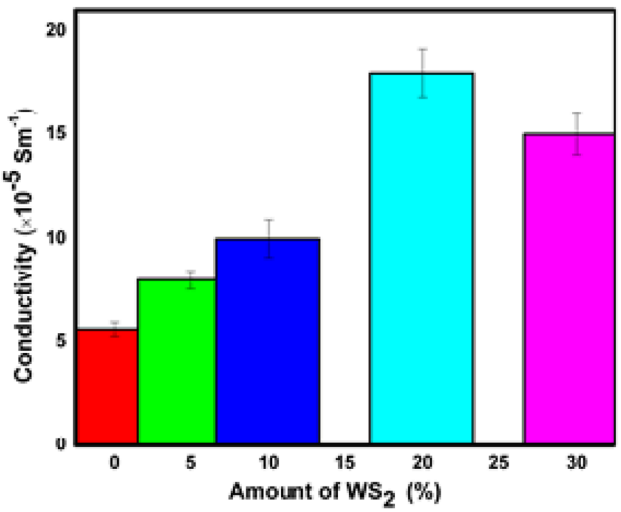

Fig. 10 DC conductivity of PNA and PNA–WS_2 nanocomposites

transport, thus diminishing its conductivity. Additionally, the decrease in chain length or conjugation in an increase in WS_2 loading could be another reason for lowering conductivity as proposed earlier reports [72, 73].Thus present study reveals that, by appropriately controlling the dispersion of WS_2, it could be possible to tune the electrical transport properties of the PNA composites.

3.10 Dielectric studies

The extent of electric charge storage and the mechanism involved in the polarization and charge storage can be understood by measuring the variation of dielectric parameters with frequency. The dielectric permittivity of a material is a complex quantity and consists of the real and imaginary parts. The real part of the dielectric permittivity (**ε′**) corresponds to dielectric permittivity, and the imaginary part (**ε″**) corresponds to dielectric loss [72]. The dielectric parameters of compressed discs of PNA and PNA–WS_2 composites are measured within the frequency range of 50–1.5 MHz. The variation of **ε′** against frequency for different compositions are presented in Fig. 11a, b. It is clear from Fig. 11a that the **ε′** of the pristine PNA and PNA–WS_2 nanocomposites are high at a lower frequency and gradually decreases as frequency increases. However, at higher frequencies **ε′** remains almost constant for a wide range of frequencies.

The dielectric properties of a heterogeneous system like PNA–WS_2 composites are dependent on the nature of the matrix and polarization behaviour is quite complicated as the components are of different conductivity and dielectric permittivity. It is reported that the dielectric permittivity of both bulk and few-layer WS_2 and MoS_2 is very low due to its low conductivity [74, 75]. Here, three different polarization mechanisms may co-exist, namely interfacial polarization, dipolar orientation and counter ion polarization. As the PNA–WS_2 composites are composed of thin layers of semiconducting WS_2 layers intercalated by conjugated PNA chains, interfacial polarization (Maxwell–Wagner–Sillar polarization) is supposed to be predominant [76]. Additionally, the counter ion polarization resulted from the displacement of charged species like dopant anions or protons under the external electric field have significant contribution towards the **ε′** of the composites. Therefore, the observed high dielectric permittivity at the low-frequency region, i.e., 100–1000 Hz is credited to the counter ion polarization. At 100 Hz, **ε′** observed for PNA–20WS_2 and PNA–30WS_2 were 5650 and 3920, respectively, which is significantly higher than the pristine PNA. At higher frequencies, the dipoles do not get enough time to align according to the rapidly changing

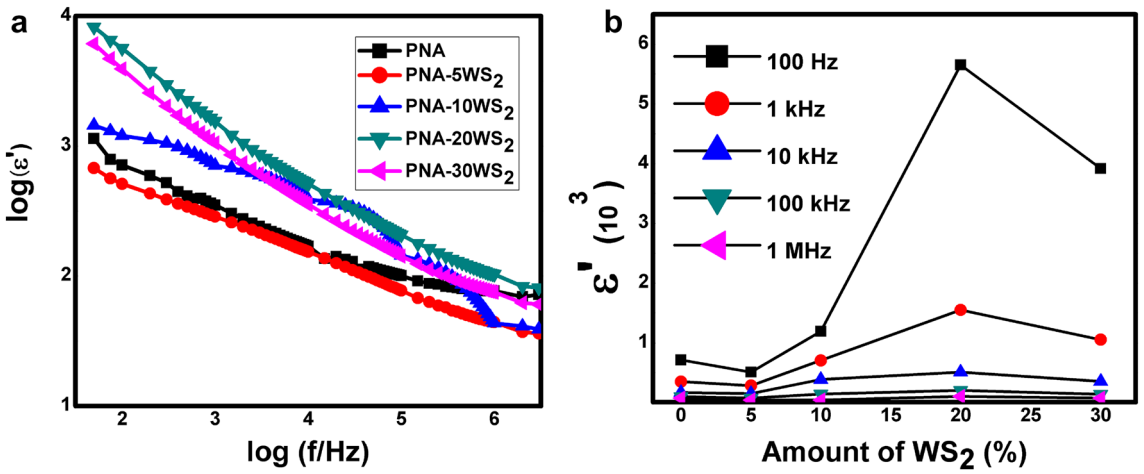

Fig. 11 Plot of variation of ε′ of PNA and PNA–WS_2 with frequency (**a**) and variation of ε′ with composition at a different frequency (**b**)

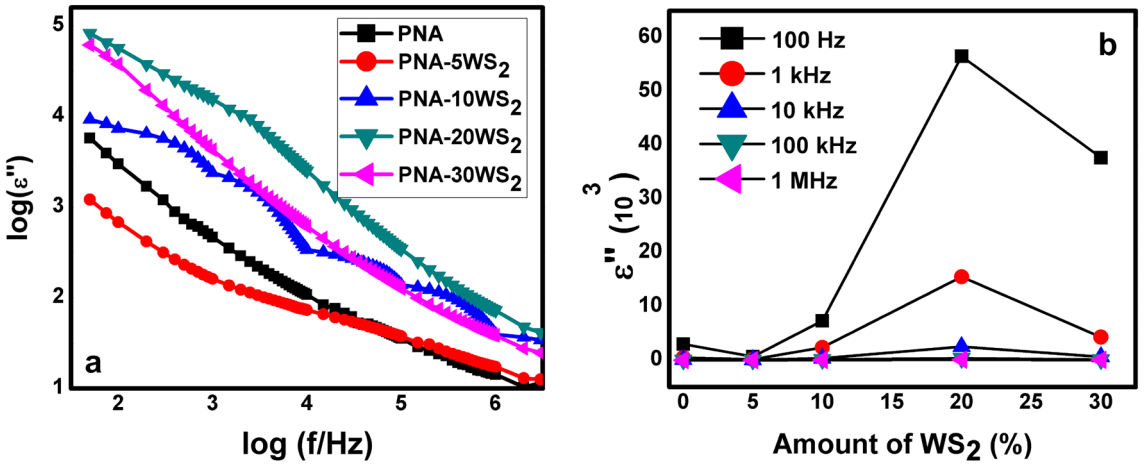

Fig. 12 Plot of variation of ε″ of PNA and PNA–WS_2 with frequency (**a**) and variation of ε″ with composition at different applied frequencies (**b**)

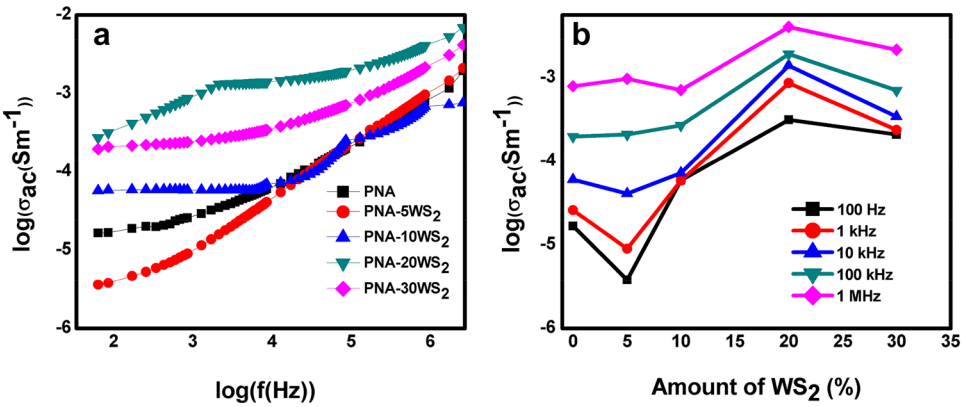

Fig. 13 Plot of variation of AC conductivity of PNA and PNA–WS_2 with frequency (**a**) and variation of AC conductivity with composition at different applied frequencies (**b**)

alternating electric fields, thus diminishing polarization resulting in a low dielectric value. It was observed that the dielectric permittivity of all systems decreased continuously as frequency increases following the general trend reported for common dielectric materials. Even though, the PNA–$20WS_2$ and PNA–$30WS_2$ nanocomposites have dielectric permittivity around 40 at 1 MHz which is due to the large interfacial polarization and the accumulation of charges at the phase boundaries of WS_2 and PNA [77]. The variation of **ε′** with % of WS_2 at different frequencies is shown in Fig. 11b. At any frequency, the **ε′** values of the pelletized samples followed the order PNA–$20WS_2$ > PNA–$30WS_2$ > PNA–$10WS_2$ > PNA > PNA–$5WS_2$. Therefore, the study reveals that the incorporation of WS_2 into PNA has a radical enhancement in dielectric parameters of the nanocomposites.

The variation of the imaginary part of dielectric permittivity **(ε″)** with frequency (logf) and composition are shown in Fig. 12a, b. It is clear from Fig. 12a, b that **ε″** and the dielectric loss values of PNA and PNA–WS_2 nanocomposites show high sensitivity to composition and frequency, especially at low-frequency regions. Figure 12b shows that variation of **ε″** with composition is similar to that of **ε′**, i.e. PNA–$20WS_2$ > PNA–$30WS_2$ > PNA–$10WS_2$ > PNA > PNA–$5WS_2$. The observed higher dielectric loss for PNA–$20WS_2$ might be accounted by the percolation and the associated growth of the conductivity tail. The observed trend in **ε″** with frequency corroborates that ionic and interfacial polarizations are mainly contributing towards the observed dielectric permittivity.

The variation of AC conductivity of PNA and PNA–WS_2 nanocomposites with applied frequency are presented in Fig. 13a, b. Similar to other dielectric parameters, conductivity values are also sensitive to the composition and applied the electric field. It is observed from Fig. 13a that AC conductivity of the doped PNA and PNA–WS_2 nanocomposites increase with the increase in an applied electric field. An increase in the applied electric field enhances the charge carriers' jumps between the localized positions; accordingly, the activation energy decreases, facilitating

charge transport, and therefore, an increased conductivity is generally observed [28, 29, 78]. AC conductivity values for PNA, PNA–5WS_2 and PNA–10WS_2 nanocomposites, which were in the range of 10^{-5} Sm^{-1} at 1000 Hz and is lower compared to other composites. The variation of AC conductivity followed presented in Fig. 13b shows that it has the same trend as that of DC conductivity, **ε″** and **ε′.** The A.C. conductivity of prepared systems followed the order PNA–20WS_2 > PNA–30WS_2 > PNA–10WS_2 > PNA > PNA–5WS_2. Among the whole composites prepared, PNA–20WS_2 and PNA–30WS_2 composites show better A.C conductivity at all frequency range and conductivity increases on an increasing frequency. The maximum conductivity observed was 4.4×10^{-3} Sm^{-1} for at 1 MHz for PNA–20WS_2, which is comparatively higher than reported PANI composites containing metals and metal chalcogenides fillers [75, 77, 79, 80]. The increased conductivity is attributed to the increase in the number of charge carriers and its diffusion through the amorphous composite matrix along with the contribution from localized polarons and bipolarons. The high conductivity values of PNA–WS_2nanocomposites suggested better transport of charge carries within and between polymer chains owing to intimate contact between the WS_2 layers and the conjugated PNA phase.

The observed composition dependence of dielectric parameters can be explained by considering micro-level capacitors like the arrangement between the conjugated PNA and semiconducting WS_2 layers as dielectric layers. The **ε′** and **ε″** values suggest a higher number of charge carries / mobile salt ions in the bulk nanocomposites. The observed high AC conductivity value also proposes a large number of charge diffusion within the amorphous region and this indicates the presence of isolated polarons in this region. On increasing the amount of WS_2 sheets, a higher number of micro capacitor arrangements are formed, thus increasing the dielectric permittivity and AC conductivity. The observed maximum conductivity, **ε′** and **ε″** for PNA–20WS_2 may be due to the maximum contribution from polar WS_2 and improved interfacial interactions. On further increasing the WS_2 content, the thickness of dielectric layers increases and more agglomeration due to restacking may occur, causing a considerable reduction in the number of micro capacitor units inside the composite matrix, following a lowering of dielectric permittivity [37, 44]. Therefore, it is proposed that dielectric phenomena of PNA–WS_2 are governed by several factors including nature, composition, interfacial interaction, area of contact, the thickness of layers, the extent of intercalation and chain length of the polymer and mechanism of conduction. For a complex heterogeneous system like this, two types of dipoles, one from the polymer and other from the WS_2 sheets, should be considered and a detailed molecular level study applying theoretical simulation analysis is required for the complete understanding of the charge storage and dissipation phenomena of such nanocomposites.

As mentioned before, WS_2 being a polar molecule can contribute to the overall polarization of the nanocomposites. However, when the amount of WS_2 added is low (for PNA–5WS_2), the addition of WS_2 might have caused the reorganization of PNA chains causing more scattering creating more voids between PNA chains and hence lowering its dielectric characteristics [81]. As we increase the WS_2 loading up to 20%, the **ε″** and value increases that maybe because of the interfacial area between the WS_2 sheets and PNA together with additional contributions from the incorporated polar WS_2. However, above 20% WS_2 loading, the **ε′** and **ε″** decreases because of the clustering of WS_2 sheets as evidenced by the SEM and TEM studies, causing corresponding decrease in the typical Maxwell–Wagner–Sillar interfacial polarization. Similar lowering of dielectric properties at higher filler loading have been reported by other authors for PANI composites containing inorganic fillers like clay, ferrite and metal oxides [37, 43, 44, 81, 82]. Therefore, it is concluded that maximum space charge distribution is observed with an optimum concentration of 20% WS_2 by weight.

The studiesq′ indicates that the dielectric characteristics can be tuned by controlling the PNA–WS_2 ratio. The high dielectric permittivity and loss values for optimum composition suggest that the PNA–WS_2 system could be useful in the capacitor application, especially in the low-frequency range and could find excellent applicability in EMI shielding.

4 Conclusion

PNA intercalated WS_2 nanocomposites with different WS_2 content have been synthesized by the in-situ chemical oxidative polymerization method. The crystal structure, surface morphology optical, thermal and electrical properties have been investigated and discussed in detail. The presence of WS_2 improves the thermal stability and nanocomposites' electrical and optical characteristics have shown intimate relation with the composition and dispersion of incorporated WS_2 layers. Improved dielectric performance is attributed to the special intercalated arrangement and synergistic electron transfer interactions between PNA and WS_2. The observed maximum dielectric loss for PNA–20WS_2 is credited to the percolation and the associated growth of the conductivity tail. Notably, the present study provides a comprehensive picture of a percolated PNA composite, and it is suggested that prepared PNA–WS_2 nanocomposites with tunable electrical and

dielectric attributes can be used for various fields, including as a capacitor, as microwave absorbing materials or in EMI shielding applications.

Acknowledgement The authors gratefully acknowledged the financial assistance to Femina K.S. granted by the University Grants Commission (under Faculty Development Programme (Grant No. FIP/12th Plan/KLMG 009 TF 12 dated 20 /04/2017), Government of India. The authors thank SAIF STIC, CUSAT, Kerala, India, for characterization facilities, Department of physics, Nirmala College, Muvattupuzha, Kerala for conductivity measurements and Department of physics, S.B College Changanassery, Kottayam, Kerala, India for dielectric measurements.

Compliance with ethical standards

Conflicts of interest The authors declare no conflict of interest to publish the paper.

References

1. Rao CNR, Matte HSSR, Subrahmanyam KS (2013) Synthesis and selected properties of graphene and graphene mimics. Acc Chem Res 46:149–159. https://doi.org/10.1021/ar300033m
2. Bai S, Xiong Y (2015) Recent advances in two-dimensional nanostructures for catalysis applications. Sci Adv Mater 7:2168–2181. https://doi.org/10.1166/sam.2015.2261
3. Feng H, Hu Z, Liu X (2015) layered materials using liquid alkali metal alloys †. Chem Commun 51:10961–10964. https://doi.org/10.1039/C5CC02625C
4. Nair JSA, Aswathi R, Sandhya KY (2019) Reverse micelle assisted hydrothermal reaction route for the synthesis of homogenous MoS_2 nanospheres. SN Appl Sci 1:508. https://doi.org/10.1007/s42452-019-0528-y
5. Cong C, Shang J, Wang Y, Yu T (2018) Optical properties of 2D semiconductor WS_2. Adv Opt Mater 6:1–15. https://doi.org/10.1002/adom.201700767
6. Pagona G, Bittencourt C, Arenal R, Tagmatarchis N (2015) Exfoliated semiconducting pure 2H-MoS2and 2H-WS2assisted by chlorosulfonic acid. Chem Commun 51:12950–12953. https://doi.org/10.1039/c5cc04689k
7. Thripuranthaka M, Kashid RV, Sekhar Rout C, Late DJ (2014) Temperature dependent Raman spectroscopy of chemically derived few layer MoS2 and WS2 nanosheets. Appl Phys Lett 104:1–5. https://doi.org/10.1063/1.4866782
8. Frey GL, Elani S, Homyonfer M et al (1998) Optical-absorption spectra of inorganic fullerenelike MS2 (M = Mo, W). Phys Rev B 57:6666–6671. https://doi.org/10.1103/PhysRevB.57.6666
9. Mao X, Xu Y, Xue Q et al (2013) Ferromagnetism in exfoliated tungsten disulfide nanosheets. Nanoscale Res Lett 8:1–6. https://doi.org/10.1186/1556-276X-8-430
10. Elías AL, Perea-López N, Castro-Beltrán A et al (2013) Controlled synthesis and transfer of large-area WS2 sheets: from single layer to few layers. ACS Nano 7:5235–5242. https://doi.org/10.1021/nn400971k
11. Park J, Kim MS, Cha E et al (2017) Synthesis of uniform single layer WS2 for tunable photoluminescence. Sci Rep 7:16121–16128. https://doi.org/10.1038/s41598-017-16251-2
12. Ovchinnikov D, Allain A, Huang YS et al (2014) Electrical transport properties of single-layer WS2. ACS Nano 8:8174–8181. https://doi.org/10.1021/nn502362b
13. De B, Kuila T, Kim NH, Lee JH (2017) Carbon dot stabilized copper sulphide nanoparticles decorated graphene oxide hydrogel for high performance asymmetric supercapacitor. Carbon N Y 122:247–257. https://doi.org/10.1016/j.carbon.2017.06.076
14. Xu W, Zhu S, Liang Y et al (2015) Nanoporous CuS with excellent photocatalytic property. Nat Publ Gr. https://doi.org/10.1038/srep18125
15. Tanveer M, Cao C, Aslam I et al (2014) Effect of the morphology of CuS upon the photocatalytic degradation of organic dyes. RSC Adv 4:63447–63456. https://doi.org/10.1039/c4ra04940c
16. Zhou KG, Mao NN, Wang HX et al (2011) A mixed-solvent strategy for efficient exfoliation of inorganic graphene analogues. Angew Che Int Ed 50:10839–10842. https://doi.org/10.1002/anie.201105364
17. Loo AH, Bonanni A, Sofer Z, Pumera M (2015) Exfoliated transition metal dichalcogenides (MoS2, MoSe2, WS2, WSe2): an electrochemical impedance spectroscopic investigation. Electrochem Commun 50:39–42. https://doi.org/10.1016/j.elecom.2014.10.018
18. Xu D, Xu P, Zhu Y et al (2018) High yield exfoliation of WS2Crystals into 1–2 layer semiconducting nanosheets and efficient photocatalytic hydrogen evolution from WS2/CdS nanorod composites. ACS Appl Mater Interfaces 10:2810–2818. https://doi.org/10.1021/acsami.7b15614
19. Vattikuti SVP, Byon C, Reddy CV (2016) Preparation and improved photocatalytic activity of mesoporous WS2using combined hydrothermal-evaporation induced self-assembly method. Mater Res Bull 75:193–203. https://doi.org/10.1016/j.materresbull.2015.11.059
20. Lan F, Yang R, Xu Y et al (2018) Synthesis of large-scale single-crystalline monolayer WS2 using a semi-sealed method. Nanomaterials. https://doi.org/10.3390/nano8020100
21. Patil BN, Acharya SA (2014) Preparation of zns-graphene nanocomposite and its photocatalytic behavior for dye degradation. Adv Mater Lett 5:113–116. https://doi.org/10.5185/amlett.2013.fdm.16
22. Kr S, Sarkar DD (2014) Effect of Zn source concentration on structural, optical and electrical properties of zinc sulphide—polyaniline (ZnS–PANI) nanocomposite thin films. J Mater Sci Mater Electron 12:5638–5645. https://doi.org/10.1007/s10854-014-2353-9
23. Allahveran S, Mehrizad A (2017) Polyaniline/ZnS nanocomposite as a novel photocatalyst for removal of Rhodamine 6G from aqueous media: optimization of influential parameters by response surface methodology and kinetic modeling. J Mol Liq 225:339–346. https://doi.org/10.1016/j.molliq.2016.11.051
24. Batool A, Kanwal F, Riaz S, et al (2015) Novel method to synthesize conducting polyaniline/nickle sulphide nanocomposite films and the study of their structural and electrical properties. In: Materials today: proceedings, pp 5201–5204
25. Lima RMAP, de Oliveira MCA, de Oliveira HP (2019) Wearable supercapacitors based on graphene nanoplatelets/carbon nanotubes/polypyrrole composites on cotton yarns electrodes. SN Appl Sci 1:325. https://doi.org/10.1007/s42452-019-0343-5
26. Chandran M, Shamna I, Anusha A, Bhagiyalakshmi M (2019) Synthesis of mesoporous carbon-polymeric hybrid material for energy storage application. SN Appl Sci 1:509. https://doi.org/10.1007/s42452-019-0509-1
27. Abdelmalik AA, Sadiq A (2019) Thermal and electrical characterization of composite metal oxides particles from periwinkle shell for dielectric application. SN Appl Sci 1:373. https://doi.org/10.1007/s42452-019-0388-5
28. Sen A (2019) Tunable dielectric properties of niobium (Nb) doped $CaCu_3Ti_4O_{12}$ nanocubes synthesized via facile molten salt route. SN Appl Sci 1:971. https://doi.org/10.1007/s42452-019-1037-8

29. Ahmad Z (2012) Polymer dielectric materials. In: Dielectric materialIntech. IntechOpen, pp 3–26. https://doi.org/10.5772/50638
30. Panda M, Mishra A, Shukla P (2019) Effective enhancement of dielectric properties in cold-pressed polyvinyledene fluoride/barium titanate nanocomposites. SN Appl Sci 1:230. https://doi.org/10.1007/s42452-019-0234-9
31. Su Y, Ba C, Wang F (2019) Improved dielectric permittivity of NBCTO/epoxy composite films with low dielectric loss. SN Appl Sci 1:1147. https://doi.org/10.1007/s42452-019-1211-z
32. Mezdour D (2017) Dielectric properties of polyaniline composites. Spectrosc Lett 50:214–219. https://doi.org/10.1080/00387010.2017.1287093
33. Pinto NJ, Shah PD, Kahol PK, McCormick BJ (1996) Dielectric constant and ac conductivity in polyaniline derivatives. Solid State Commun 97:1029–1031. https://doi.org/10.1016/0038-1098(95)00853-5
34. Singh R, Bajpai AK, Shrivastava AK (2019) CdSe QDs reinforced poly(1, 8 diaminonaphthalene) (PDAN) offers improved thermal and AC conductivity properties. SN Appl Sci 1:815. https://doi.org/10.1007/s42452-019-0835-3
35. Khatoon H, Iqbal S, Ahmad S (2019) Influence of medium on structure, morphology and electrochemical properties of polydiphenylamine/vanadium pentoxide composite. SN Appl Sci 1:261. https://doi.org/10.1007/s42452-019-0285-y
36. Pant HC, Patra MK, Negi SC et al (2006) Studies on conductivity and dielectric properties of polyaniline-zinc sulphide composites. Bull Mater Sci 29:379–384. https://doi.org/10.1007/BF02704139
37. Vellakkat M, Kamath A, Raghu S et al (2014) Dielectric constant and transport mechanism of percolated polyaniline nanoclay composites. Ind Eng Chem Res 53:16873–16882. https://doi.org/10.1021/ie502922b
38. Huang KJ, Wang L, Liu YJ et al (2013) Layered MoS_2-graphene composites for supercapacitor applications with enhanced capacitive performance. Int J Hydrogen Energy 38:14027–14034. https://doi.org/10.1016/j.ijhydene.2013.08.112
39. Liu H, Zhang F, Li W et al (2015) Porous tremella-like MoS_2/polyaniline hybrid composite with enhanced performance for lithium-ion battery anodes. Electrochim Acta 167:132–138. https://doi.org/10.1016/j.electacta.2015.03.151
40. Peng S, Fan L, Wei C et al (2017) Flexible polypyrrole/copper sulfide/bacterial cellulose nanofibrous composite membranes as supercapacitor electrodes. Carbohydr Polym 157:344–352. https://doi.org/10.1016/j.carbpol.2016.10.004
41. Kruefu V, Wisitsoraat A, Tuantranont A, Phanichphant S (2014) Gas sensing properties of conducting polymer/Au-loaded ZnO nanoparticle composite materials at room temperature. Nanoscale Res Lett. https://doi.org/10.1186/1556-276X-9-467
42. Sasikala R, Gaikwad AP, Jayakumar OD et al (2015) Nanohybrid MoS_2-PANI-CdS photocatalyst for hydrogen evolution from water. Colloids Surf A Physicochem Eng Asp 481:485–492. https://doi.org/10.1016/j.colsurfa.2015.06.027
43. Faisal M, Khasim S (2013) Polyaniline-antimony oxide composites for effective broadband EMI shielding. Iran Polym J (Engl Ed) 22:473–480. https://doi.org/10.1007/s13726-013-0149-z
44. Patil R, Roy AS, Anilkumar KR et al (2012) Dielectric relaxation and ac conductivity of polyaniline-zinc ferrite composite. Compos Part B Eng 43:3406–3411. https://doi.org/10.1016/j.compositesb.2012.01.090
45. Heinemann E, Strategic S, Officer P et al (2011) Nanocomposites of poly(1-naphthylamine)/SiO2 and poly(1-naphthylamine)/TiO2: comparative photocatalytic activity evaluation towards methylene blue dye. J Macromol Sci Part B Phys 10:311–317. https://doi.org/10.1007/s10965-010-9420-6
46. Riaz U, Ahmad S, Ashraf SM (2009) Comparison of corrosion protective performance of nanostructured polyaniline and poly(1-naphthylamine)-based alkyd coatings on mild steel. Mater Corros 60:280–286. https://doi.org/10.1002/maco.200805054
47. Ameen S, Akhtar MS, Kim YS et al (2010) Synthesis and characterization of novel poly(1-naphthylamine)/zinc oxide nanocomposites: application in catalytic degradation of methylene blue dye. Colloid Polym Sci 288:1633–1638. https://doi.org/10.1007/s00396-010-2284-9
48. Riaz U, Ashraf SM, Farooq M (2015) Effect of pH on the microwave-assisted degradation of methyl orange using poly(1-naphthylamine) nanotubes in the absence of UV–visible radiation. Colloid Polym Sci 293:1035–1042. https://doi.org/10.1007/s00396-014-3485-4
49. Riaz U, Ahmad S, Ashraf SM (2008) Template free synthesis of nanoparticles of poly (1-naphthylamine): influence of alcoholic medium on polymerization. Colloid Polym Sci 286:459–462. https://doi.org/10.1007/s00396-007-1803-9
50. Riaz U, Ashraf SM, Budhiraja V et al (2016) Comparative studies of the photocatalytic and microwave -assisted degradation of alizarin red using ZnO/poly(1-naphthylamine) nanohybrids. J Mol Liq 216:259–267. https://doi.org/10.1016/j.molliq.2016.01.018
51. Riaz U, Ahmad S, Ashraf SM (2008) Effect of dopant on the nanostructured morphology of poly (1-naphthylamine) synthesized by template free method. Nanoscale Res Lett 3:45–48. https://doi.org/10.1007/s11671-007-9112-2
52. Riaz U, Ahmad S, Ashraf SM (2008) Pseudo template synthesis of poly (1-naphthylamine): effect of environment on nanostructured morphology. J Nanoparticle Res 10:1209–1214. https://doi.org/10.1007/s11051-007-9356-x
53. Riaz U, Ahmad S, Ashraf SM (2008) Influence of polymerization conditions on the template free synthesis of nanoparticles of poly (1-naphthylamine). Polym Bull 60:487–493. https://doi.org/10.1007/s00289-008-0886-x
54. Riaz U, Ashraf SM (2013) Evaluation of antibacterial activity of nanostructured copolymers of poly (naphthylamine). Int J Polym Mater Polym Biomater 62:406–410. https://doi.org/10.1080/00914037.2012.719140
55. Saidu FK, Joseph A, Varghese EV, Thomas GV (2019) Characterization and electrochemical studies on poly(1-naphthylamine)-graphene oxide nanocomposites prepared by in situ chemical oxidative polymerization. J Solid State Electrochem 23:2897–2906. https://doi.org/10.1007/s10008-019-04380-9
56. Manjunatha S, Rajesh S, Vishnoi P, Rao CNR (2017) Reaction with organic halides as a general method for the covalent functionalization of nanosheets of 2D chalcogenides and related materials. J Mater Res 32:2984–2992. https://doi.org/10.1557/jmr.2017.224
57. Jha R, Santra S, Guha PK (2016) Green synthesis route for WS2 nanosheets using water intercalation. Mater Res Express 3:1–10. https://doi.org/10.1088/2053-1591/3/9/095014
58. Xu B, Lin B, Chen Z et al (2009) Preparation and electrical conductivity of polypyrrole/WS_2 layered nanocomposites. J Colloid Interface Sci 330:220–226. https://doi.org/10.1016/j.jcis.2008.10.033
59. Riaz U, Ahmad S, Ashraf SM (2008) Influence of polymerization conditions on the template free synthesis of nanoparticles of poly (1-naphthylamine). Polym Bull 493:487–493. https://doi.org/10.1007/s00289-008-0886-x
60. Massoumi B, Entezami AA, Aghili H (2011) Conductivity and solubility of nanostructure poly(α-naphthylamine). Iran Polym J 20:295–303
61. Riaz U, Ahmad S, Ashraf SM (2008) Template polymerization of nano-scale poly(1-naphthylamine): effect of oxidant on the spectral, thermal and morphological characteristics. Des Monomers Polym 11:201–214. https://doi.org/10.1163/156855508X298099

62. Fan L, Suni II (2017) Electrodeposition and capacitance measurements of WS_2 thin films. J Electrochem Soc 164:D681–D686. https://doi.org/10.1149/2.0711712jes
63. Jha RK, Wan M, Jacob C, Guha PK (2018) Ammonia vapour sensing properties of in situ polymerized conducting PANI-nanofiber/WS_2 nanosheet composites. New J Chem 42:735–745. https://doi.org/10.1039/c7nj03343e
64. Rohaizad N, Mayorga-Martinez CC, Sofer Z, Pumera M (2017) 1T-phase transition metal dichalcogenides (MoS_2, $MoSe_2$, WS_2, and WSe_2) with fast heterogeneous electron transfer: application on second-generation enzyme-based biosensor. ACS Appl Mater Interfaces 9:40697–40706. https://doi.org/10.1021/acsami.7b13090
65. Chen TY, Chang YH, Hsu CL et al (2013) Comparative study on MoS_2 and WS_2 for electrocatalytic water splitting. Int J Hydrogen Energy 38:12302–12309. https://doi.org/10.1016/j.ijhydene.2013.07.021
66. Riaz U, Ashraf SM, Aleem S et al (2016) Microwave-assisted green synthesis of some nanoconjugated copolymers: characterisation and fluorescence quenching studies with bovine serum albumin. New J Chem 40:4643–4653. https://doi.org/10.1039/c5nj02513c
67. Jadoun S, Ashraf SM, Riaz U (2017) Tuning the spectral, thermal and fluorescent properties of conjugated polymers: via random copolymerization of hole transporting monomers. RSC Adv 7:32757–32768. https://doi.org/10.1039/c7ra04662f
68. Raghu MS, Kumar KY, Rao S et al (2018) Fabrication of polyaniline–few-layer MoS_2 nanocomposite for high energy density supercapacitors. Polym Bull 75:4359–4375. https://doi.org/10.1007/s00289-017-2267-9
69. Huang KJ, Wang L, Liu YJ et al (2013) Synthesis of polyaniline/2-dimensional graphene analog MoS_2 composites for high-performance supercapacitor. Electrochim Acta 109:587–594. https://doi.org/10.1016/j.electacta.2013.07.168
70. Cattarin S, Doubova L, Mengoli G, Zotti G (1988) Electrosynthesis and properties of ring-substituted polyanilines. Electrochim Acta 33:1077–1084. https://doi.org/10.1016/0013-4686(88)80198-1
71. Voldman A, Zbaida D, Cohen H, et al (2007) A nanocomposite of polyaniline/inorganic nanotubes. Macromol Chem Phys 2007–2015. https://doi.org/10.1002/macp.201300283
72. Wang J, Wu Z, Hu K et al (2015) High conductivity graphene-like MoS_2/polyaniline nanocomposites and its application in supercapacitor. J Alloys Compd 619:38–43. https://doi.org/10.1016/j.jallcom.2014.09.008
73. Sun J, Shen Y, Hu X-S (2018) Polyaniline/flower-like CuS composites with improved electromagnetic interference shielding effectiveness. Polym Bull 75:653–667. https://doi.org/10.1007/s00289-017-2060-9
74. Liang L, Meunier V (2014) First-principles Raman spectra of MoS_2, WS_2 and their heterostructures. Nanoscale 6:5394–5401. https://doi.org/10.1039/c3nr06906k
75. Zhang WL, Jiang D, Wang X et al (2017) Growth of polyaniline nanoneedles on MoS_2 nanosheets, tunable electroresponse, and electromagnetic wave attenuation analysis. J Phys Chem C 121:4989–4998. https://doi.org/10.1021/acs.jpcc.6b11656
76. Vu TTN, Teyssedre G, Le RS, Laurent C (2017) Maxwell–Wagner effect in multi-layered dielectrics: interfacial charge measurement and modelling. Technologies 5:27. https://doi.org/10.3390/technologies5020027
77. Choudhury A (2009) Polyaniline/silver nanocomposites: dielectric properties and ethanol vapour sensitivity. Sens Actuators B Chem 138:318–325. https://doi.org/10.1016/j.snb.2009.01.019
78. Rui-ting MA, Vellakkat M, Kamath A et al (2014) Frequency dependence of dielectric properties and conductivity of bulk copper sulfide. Mater Sci Semicond Process 18:141–145. https://doi.org/10.1016/j.mssp.2013.11.006
79. Zhu J, Wei S, Zhang L et al (2011) Electrical and dielectric properties of polyaniline–Al_2O_3 nanocomposites derived from various Al_2O_3 nanostructures. J Mater Chem 21:3952–3959. https://doi.org/10.1039/c0jm03908j
80. Ur Rehman S, Liu J, Ahmed R, Bi H (2018) Synthesis of composite of ZnO spheres with polyaniline and their microwave absorption pro perties. J Saudi Chem Soc 23:6. https://doi.org/10.1016/j.jscs.2018.04.006
81. Sharma BK, Gupta AK, Khare N et al (2009) Synthesis and characterization of polyaniline-ZnO composite and its dielectric behavior. Synth Met 159:391–395. https://doi.org/10.1016/j.synthmet.2008.10.010
82. Dutta K, De SK (2006) High dielectric permittivity in silica-polyaniline nanocomposites. J Nanosci Nanotechnol 6:499–504. https://doi.org/10.1166/jnn.2006.091